

# Chaos and rotational damping in particle-rotor model

Javid A. Sheikh<sup>1,2</sup> and Yang Sun<sup>3,4,5</sup>

<sup>1</sup> *Physik-Department, Technische Universität München, D-85747 Garching, Germany*

<sup>2</sup> *Department of Physics, University of Kashmir, Hazrathbal, Srinagar, Kashmir, 190 006, India*

<sup>3</sup> *Department of Physics, University of Notre Dame, Notre Dame, Indiana 46556, U.S.A.*

<sup>4</sup> *Department of Physics, Tsinghua University, Beijing 100084, P.R. China*

<sup>5</sup> *Department of Physics, Xuzhou Normal University, Xuzhou, Jiangsu 221009, P.R. China*

---

## Abstract

The onset of chaos and the mechanism of rotational damping are studied in an exactly soluble particle-rotor model. It is shown that the degree of chaoticity as inferred from the statistical measures is closely related to the onset of rotational damping obtained using the model Hamiltonian.

---

## 1 Introduction

The study of quantum chaos in many-body problems using the random matrix theory (RMT) [1] is now an established field of research in physics [2,3]. It is known that the statistical properties of a quantum many-body system which follow the predictions of RMT have chaotic behaviour in the classical phase space [4]. This behaviour of a quantum many-body system was first observed for the neutron resonance states of compound nuclei [5]. It was shown that the fluctuation properties of the neutron resonance states follow the Gaussian Orthogonal Ensemble (GOE) statistics which is one of universal classes of RMT. The statistical analysis of the nuclear states which are populated through  $\gamma$ -decay has also been performed [6–14]. It has been demonstrated using different theoretical approaches that at low-excitation energies the statistical analysis depicts a Poissonian distribution which corresponds to underlying regular classical motion. However, at high-excitation energy the distribution follows the

GOE statistics, implying that the underlying classical motion is chaotic. This correlation between the statistical distribution and the classical motion has been obtained for a large class of physical systems [3].

However, the important question in the study of quantum chaos, which has remained largely unanswered, is: *what are the consequences of quantum chaos in measurable quantities?* It has recently been demonstrated [8] that, in a nuclear system, the overlap-integral between the wave functions of the neighbouring rotational states can provide a measure of the degree of chaoticity. However, the overlap-integral is not directly a measurable quantity. What is needed to be calculated is the electromagnetic-transitions between the two states. In the previous work [8], the cranking mean-field model was used to calculate the overlaps. The cranking wave function does not have a well-defined angular momentum, and in principle, is not appropriate to study the electromagnetic transition probabilities. In order to avoid any errors due to usage of mean-field approximation, in the present work, we have developed a particle-rotor model (PRM) approach in which angular momentum is strictly conserved. We would like to use the PRM wave functions to study the consequences of the chaotic motion on the electromagnetic transitions.

It should be mentioned that the question of rotational damping has also been addressed recently by other authors [9–11] and it has been shown that the phenomenon of rotational damping observed in deformed nuclei is a possible manifestation of quantum chaos. In these analysis, the rotational bands were obtained as the intrinsic excitations of a Cranked-Nilsson mean-field potential. In order to obtain the rotational damping, the bands were mixed using a two-body residual interaction. Since in the cranked mean-field approaches, as already mentioned, angular momentum is not a conserved quantity, these calculations are suitable for very high-spin states for which cranking becomes a good approximation to the angular momentum projection method.

The purpose of the present work is to present an alternative analysis of the rotational damping using the particle-rotor model. Pairing is explicitly included in the present calculations and, therefore, the results discussed are applicable to all the spin regimes. Furthermore, we use the same Hamiltonian for obtaining the bands structures as well as the rotational damping. In the earlier studies [9–11], the Nilsson potential was used to obtain the intrinsic bands and the rotational damping was then calculated with a residual two-body interaction.

The exact analysis in the PRM limits the configuration space that can be employed in the numerical studies. Therefore, we shall work in a model space of a deformed single-j shell as has been done in the earlier studies [7,8]. This would imply that our results cannot be compared directly with the experimental data. The main essence of the present work would be to draw a connection

between the mechanism of rotational damping and the chaotic features in an exactly soluble model.

The manuscript is organized as follows: In the next section, we give some relevant details of the PRM. The PRM is a standard model and the discussion of this approach can be found in the textbooks, for example in Ref. [15]. We shall, therefore, only give the relevant expressions for the quantities which are used in the present work. The results of the calculations are presented and discussed in section III. Finally, the present study is summarized in section IV.

## 2 Particle-rotor model

The basic philosophy of the PRM [15] is to consider the nucleus as a core with a few valance particles. In most of the cases, the core is assumed to be inert with fixed properties. The Hamiltonian of the PRM is written as the rotor plus the particle part

$$\hat{H} = \hat{H}_{rot} + \hat{H}_{part}, \quad (1)$$

with

$$\hat{H}_{rot} = \frac{\hat{R}^2}{2\theta}. \quad (2)$$

The quantity  $\theta$  in Eq. (2) is the moment of inertia of the core and  $\hat{R}$  is the angular momentum of the core. In the present work, we shall consider the axially-symmetric core with the z-axis as the symmetry-axis.  $\hat{H}_{rot}$  in Eq. (2) can be explicitly rewritten as

$$\hat{H}_{rot} = \frac{(\hat{R}_1^2 + \hat{R}_2^2)}{2\theta} = \frac{(\hat{I}^2 - \hat{I}_3^2)}{2\theta} + \frac{(\hat{J}^2 - \hat{J}_3^2)}{2\theta} - \frac{(\hat{I}_+ \hat{J}_- + \hat{I}_- \hat{J}_+)}{2\theta}, \quad (3)$$

where  $\hat{I} = \hat{R} + \hat{J}$  is the total angular momentum and  $\hat{J}$  is the angular momentum of the valance particles. The particle part of the Hamiltonian (1) is given by

$$\hat{H}_{part} = -4\kappa \sqrt{\frac{4\pi}{5}} \hat{Y}_{20} - g\delta(\hat{r}_1 - \hat{r}_2). \quad (4)$$

The strength of the two-body interaction is  $G = g \int R_{nl}^4 r^2 dr$ . It should be noted that the delta-interaction used in the present work has predominant

pairing properties. However, since we solve the two-body interaction exactly, it will contribute to both pairing or particle-particle channel as well as to the particle-hole channel. The deformation energy  $\kappa$  is related to the deformation parameter  $\beta$  through [16]

$$\kappa \simeq 0.16\hbar\omega_0(N + 3/2)\beta, \quad (5)$$

where  $\hbar\omega_0$  is the harmonic oscillator frequency of the deformed potential and  $N$  the quantum number of the major shell. For the case of  $i_{13/2}$  shell,  $\kappa=2.5$  approximately corresponds to  $\beta = 0.28$ .

The wave function of the PRM is given by

$$|\Psi_{IM}\rangle = \sum_{K_i} c_{K_i} |IMK_i\rangle, \quad (6)$$

where

$$|IMK_i\rangle = \sqrt{\frac{2I+1}{16\pi^2(1+\delta_{K0})}} \left\{ D_{MK}^{*I} |\phi_{K_i}\rangle + (-1)^I e^{-i\pi\hat{J}_1} D_{M-K}^{*I} |\phi_{K_i}\rangle \right\}. \quad (7)$$

The wave function  $|\phi_{K_i}\rangle$  is the solution of the intrinsic particle Hamiltonian,  $H_{part}$ . For  $K = 0$ , these states have well-defined symmetry with respect to rotation about the x-axis,  $e^{-i\pi\hat{J}_1}$ .

The wave function obtained by diagonalizing the Hamiltonian, Eq. (1), is used to evaluate the electromagnetic transition probabilities. The reduced electric transition probability B(EL) from an initial state ( $I_i$ ) to a final state ( $I_f$ ) is given by

$$B(EL, I_i \rightarrow I_f) = \frac{1}{2I_i + 1} \left| \langle \Psi_{I_f} | \hat{Q}_L | \Psi_{I_i} \rangle \right|^2, \quad (8)$$

where the reduced matrix element can be expressed as

$$\begin{aligned} & \langle \Psi_{I_f} | \hat{Q}_L | \Psi_{I_i} \rangle \\ &= \sqrt{(2I_i + 1)} \sum_{K_i, K_f} c_{I_i K_i} c_{I_f K_f} \left\{ \frac{1}{\sqrt{(1 + \delta_{K_i 0})(1 + \delta_{K_f 0})}} \right. \\ & \times \sum_{q'} \left[ \begin{array}{ccc} I_i & L & I_f \\ K_i & q' & K_f \end{array} \right] \langle \phi_{K_f} | \hat{Q}_{q'}^L(\text{int}) | \phi_{K_i} \rangle \end{aligned}$$

$$\begin{aligned}
& + (-1)^{I_i} \left[ \begin{array}{ccc} I_i & L & I_f \\ -K_i & q' & K_f \end{array} \right] \langle \phi_{K_f} | \hat{Q}_{q'}^L(\text{int}) | e^{-i\pi J_1} \phi_{K_i} \rangle \\
& + \delta_{K_i K_f} Q_0 \left[ \begin{array}{ccc} I_i & L & I_f \\ K_i & 0 & K_f \end{array} \right] \Bigg\}. \tag{9}
\end{aligned}$$

The quantity  $\langle \phi_{K_f} | \hat{Q}_{q'}^L(\text{int}) | \phi_{K_i} \rangle$  is the matrix-element of the quadrupole operator in the intrinsic frame, which can be readily calculated using the wave function of the particle Hamiltonian  $\hat{H}_{part}$ .  $Q_0$  in Eq. (9) is the quadrupole moment of the core.

### 3 Results and discussions

The PRM calculations have been performed for six valance particles with the standard parameters :  $G = 0.45$  MeV and  $\theta = 24 \hbar^2$  MeV<sup>-1</sup>. These parameters have been used in most of the earlier studies and are considered to be reasonable for the  $j = 13/2$  model space [17]. In order to study the deformation dependence, the PRM calculations have been done with two sets of deformation values,  $\kappa = 2.5$  and 6.0 MeV. These deformation values correspond to the normal and superdeformed shapes. The results of the statistical analysis and the rotational damping are presented in the following subsections.

#### 3.1 Statistical analysis

The spectral rigidity statistics of Dyson and Mehta [1],  $\bar{\Delta}_3(L)$ , measures the long-range correlation of the unfolded levels

$$\Delta_3(X, L) = \min \frac{1}{L} \int_X^{X+L} [N_u(E) - (AE + B)]^2 dE, \tag{10}$$

where  $N_u$  is the cumulative level density of the unfolded levels  $X_i$ . We average  $\Delta_3(X, L)$  over intervals  $(X, X + L)$  to obtain  $\bar{\Delta}_3(L)$ , in a way as outlined in Refs. [4,18]. For ordered systems  $\bar{\Delta}_3(L) = L/15$ , and for fully chaotic ones  $\bar{\Delta}_3(L) \approx \ln(L)/\pi^2 - 3/4$  for  $L \gg 1$ . The explicit calculation of the spectral rigidity was done with the method described in Ref. [19].

In Figs. 1 and 2, the results of spectral statistics are respectively presented for the two deformation values of  $\kappa = 2.5$  and 6.0 MeV. The results with all the eigen-values are shown by filled circles. In order to study the degree of

chaoticity as a function of excitation-energy, the statistical analysis has also been studied for three more sets of eigen-values. Instead of choosing the energy window, we have considered the number of eigen-values, since the number of states in a given energy window change as a function of angular momentum and deformation. Furthermore, in order to have a reasonable statistics we have chosen 400 eigen-values in each bin. The results of the analysis with eigen-values ranging from 1 to 400 are shown by upper triangles and the third set with eigen-values from 401 to 800 are shown by lower triangles in Figs. 1 and 2. We also performed the analysis of the eigen-values ranging from 801 to 1200, but the results turn out to be very similar to the set of 401 to 800 and are not shown in the figures.

For the results for  $\kappa = 2.5$  MeV, corresponding to normal deformation, Fig. 1 indicates that at low-spin values of  $I = 10$  and  $12$ ,  $\Delta_3$  values closely follow the curve expected for the GOE distribution. It is noted that the GOE statistics is obtained at all excitation energies. Therefore, the classical motion is fully chaotic for low-spin values. For high angular momenta close to  $I = 60$ , the results with all the eigen-values deviate from the GOE curve and, therefore, indicating that the underlying classical motion is less chaotic. However, the results also show that the motion becomes more chaotic at higher excitation energies. The  $\Delta_3$  values for the set 401-801 eigen-values, shown by lower triangles, are more close to the curve expected for the chaotic motion. The generic property that the system tends to become regular with increasing angular momenta is a consequence [7] of the decoupling of the particle spins from the deformation axis of the rotor. As the nuclear system rotates faster, more and more particles tend to align their spins along the same direction of the rotation axis, which causes the system to become more regular. The results for the intermediate spin values of  $I = 30$  and  $32$  appear slightly less chaotic as compared to  $I = 10$  and  $12$ , when considering all the eigen-values, but are similar to low-spin values at higher excitation energies.

In Fig. 2, the results for  $\kappa = 6.0$  MeV, corresponding to superdeformation, indicate that for the low spin values of  $I = 10$  and  $12$ , the motion is less chaotic as compared to Fig. 1. At low-excitation energy, the results appear significantly less chaotic, but at higher excitation energy the motion tends to become chaotic. At higher spins, the results appear to be similar to those of Fig. 1.

### 3.2 *Distribution of E2 transitions*

At low excitation energies, the E2 transition from a given state populates one particular state at a lower-spin. However, at high-excitation energies, it is known that a given state populates several states. This fragmentation of the

E2 strength is referred to as the rotational damping. It has been shown using the cranking model that the onset of rotational damping at a given excitation energy is related to the underlying chaotic motion [9–11]. In the present work, we shall also try to investigate this relationship.

In order to evaluate rotational damping, the  $B(E2)$  values have been calculated for a range of initial and final states. We considered three sets of initial states, which represent the three energy sets considered in the statistical analysis of the eigen-values in Figs. 1 and 2. The three sets of initial states considered are : (a) from 1 to 50, (b) from 275 to 325 and (c) from 575 to 625. The decay of each of these initial states has been calculated to all the final states at a lower-spin. In Figs. 3 and 4, the results of  $B(E2)$  values, for the normal deformation value of  $\kappa = 2.5$  MeV, are plotted for three initial states of 26, 300 and 600 as a representative examples of the above three chosen sets. In the evaluation of the  $B(E2)$  value from Eq. (9), the quadrupole-moment of the core,  $Q_0$ , needs to be specified. In order to study the core dependence of the rotational damping, two sets of calculations have been carried out - one with no core quadrupole-moment and the other with a  $Q_0 = 2.5$  barn. The results of these two sets are shown in Figs. 3 and 4, respectively.

The results of the  $B(E2)$  for  $i = 26$  depict a peak value at around the final state  $f = 26$ , with very small contribution from the neighboring final states. For the initial state of  $i = 300$ , the  $B(E2)$  is very fragmented; there are many states to which this state decays into. For the initial state of  $i = 600$ , the fragmentation is even higher. On comparing the results of three transitions of  $I_i = 12 \rightarrow I_f = 10$ ,  $I_i = 32 \rightarrow I_f = 30$  and  $I_i = 62 \rightarrow I_f = 60$  in Fig. 1, it is noted that the degree of fragmentation decreases with increasing angular momentum.

The  $B(E2)$  results with a core quadrupole moment of  $Q_0 = 2.5$  barn, shown in Fig. 4, depict a substantially reduced fragmentation as compared to Fig. 3. The  $B(E2)$  value peaks for one particular transition for which the initial state is same as that of the final state. This can be easily understood from Eq. (9), since for the core contribution only the diagonal term for which  $K_i = K_f$  contributes. The fragmentation arises from the terms of the intrinsic quadrupole operator ( $Q_{\pm 1}, Q_{\pm 2}$ ) of Eq. (9), which mix different K-components in the intrinsic wave function.

The results for  $\kappa = 6.0$  MeV are shown in Figs. 5 and 6. Fig. 5 presents the results with no core quadrupole moment and Fig. 6 depicts the results with  $Q_0 = 5$  barn. At low excitation energies, it is noted from Fig. 5 that the fragmentation is reduced as compared to Fig. 3, but at higher excitation energies the results for the two deformation values are very similar. This observation is consistent with that obtained with the statistical analysis. The results of Fig. 6 with core quadrupole moment,  $Q_0 = 5$  barn, show that fragmentation

is substantially reduced for most of the cases.

Chaos is expected to set in when the average level distance is of the order of the coupling matrix elements [9]. In a model study with a limited model space and effective interactions which depend on parameters, it is instructive to study the density of states as a function of excitation energy and angular momentum, and the interplay of the density of states and the residual interactions in the determination of the chaotic motion.

In Fig. 7, the density of states is plotted by counting energy levels in an energy window of 1 MeV for each excitation energy. All the levels generated in the present model space are included, without any truncation. The density is shown for three angular momenta  $I = 10, 30,$  and  $60,$  and for the two deformation values of  $\kappa = 2.5$  and  $6.0$  MeV. The curves for the normally deformed case with  $\kappa = 2.5$  show a significantly decreasing trend when angular momentum increases. For the superdeformed case with  $\kappa = 6.0,$  the decreasing trend is not as pronounced as the normal deformed case. However, a drop at  $I = 60$  is still clearly seen. Comparing the results for the two deformations, we see that for the superdeformed case, the density of states is much smaller. This is particularly true for  $I = 10$  and  $30.$

If the density of states decreases with deformation, a larger residual interaction would be needed to obtain a similar amount of fragmentation in E2 strength. It is thus interesting to investigate situations in the superdeformed case, but with enhanced interactions. In Figs. 8 and 9, the same calculations presented in Figs. 5 and 6 are repeated by using a larger residual interaction. The interaction strength  $g$  in Eq. (4) is enhanced by a factor of 2. It can be seen that with the enhanced interaction, a stronger fragmentation is now obtained. The superdeformed results with enhanced interaction (Figs. 8 and 9) seem to approach the normally deformed results with the ordinary interaction (Figs. 3 and 4).

### 3.3 Rotational damping

Rotational damping is measured through the branching parameter  $n$  [10]

$$n = \left\{ \sum_j [B(E2, I_i \rightarrow I_j)]^2 \right\}^{-1}, \quad (11)$$

where  $B(E2, I_i \rightarrow I_j)$  transition probability is defined in Eqs. (8) and (9). In order to evaluate  $n,$  it is required to calculate the B(E2) transition from one particular state to all the states which are allowed by the selection rules of the  $\gamma$ -ray radiation. Considering a case where it decays to only one state

(as is true at low-excitation energy),  $n$  is equal to one if the  $B(E2)$ 's are normalized. For the case where a given state decays to two possible states with equal probabilities,  $n$  is equal to 2. This implies that for  $n$  less than 2, the band structure is discrete and each given state decays only to one state at a lower excitation energy.  $n$  greater than 2 corresponds to rotational damping, signifying that  $B(E2)$  transition strength from a given state populates two or more states at a lower spin.

The branching parameter  $n$  for  $\kappa = 2.5$  MeV is presented in Table I for a range of initial states. In order to avoid local fluctuations, the  $n$  value has been calculated by averaging over the neighboring states. In Table I, the number 1–10 in the first column, for example, indicates that  $n$  has been calculated by averaging over the initial eigen-states from 1 to 10. Of course, all possible final states have been used to calculate  $n$  from each initial state before averaging.

The second column of Table I gives the results of  $n$  for the transition  $I_i = 12 \rightarrow I_f = 10$ . It is observed from Table I that  $n$  with no core quadrupole moment becomes greater than 2 even at a very low excitation energy and increases with increasing excitation energy. For the case with a core quadrupole moment,  $Q_0 = 2.5$  barn, there is no damping at low-excitation energy and  $n$  increases very slowly as compared to the case with no quadrupole moment. This suppression of the rotational damping with a core contribution indicates that the damping is essentially determined by the contribution of valence particles.

For the second set of initial states from  $i = 275$  to 324, the value of  $n$  has now increased to more than 100 and for the third set of states from  $i = 575$  to 625,  $n$  has increased further. In general, we note that  $n$  increases with increasing excitation energy. However, for the case 615–625,  $n$  has in fact decreased. This drop in  $n$  can be understood from the fact that the present model space is finite, and as we reach the top of the shell, the level density decreases [7]. In a realistic model, the level density should increase with increasing excitation energy.

In the third column of Table I,  $n$  is given for the transition  $I_i = 32 \rightarrow I_f = 30$ .  $n$  is now reduced as compared to the transition  $I_i = 12 \rightarrow I_f = 10$ . In the last column, the results are presented for the transition  $I_i = 62 \rightarrow I_f = 60$ . The numbers are now considerably reduced. For the results with a core quadrupole moment,  $Q_0 = 2.5$ , rotational damping is completely absent at low excitation energy,  $n$  is less than 2 for almost all the first set of states.

The results of the rotational damping for  $\kappa = 6$  MeV are presented in Table II for the three transitions as studied for  $\kappa = 2.5$  MeV. For the transition  $I_i = 12 \rightarrow I_f = 10$  the damping is observed at a higher excitation energy. For the transitions  $I_i = 32 \rightarrow I_f = 30$  and  $I_i = 62 \rightarrow I_f = 60$ , the results appear

to be similar to Table I. These findings are consistent with the conclusion drawn in the previous figures. Our calculations with enhanced interaction strength for  $\kappa = 6$  MeV clearly indicate an increased damping. For example, the branching numbers  $n$  averaged for the initial eigen-states from 41 to 50 in the transition of  $I_i = 62 \rightarrow I_f = 60$  were 6.83 when  $Q_0 = 0$ , and 1.50 when  $Q_0 = 5.0$  (see Table II). With enhanced interaction, they increase to 8.20 and 1.65, respectively.

## 4 Summary and conclusions

In the present study, we tried to address a fundamental issue on the *observable consequences of quantum chaos in rotating nuclei*. It is now well accepted that the statistical analysis of a quantum many-body system can provide the important information on the underlying motion. In case that the statistical distribution follows GOE statistics, the underlying motion is considered to be chaotic, and for the case where the statistical distribution is Poissonian, the underlying motion is regarded to be regular. This statistical distribution has been studied for a wide range of physical systems. For the case of rotating nuclei, it is known that at low-excitation energy, the motion is regular, but with increasing excitation energy the motion tends to become chaotic. The angular momentum dependence of the statistical distribution has also been studied and it has been shown that for low angular momenta, the distribution follows GOE and for higher angular momenta the distribution is Poissonian.

The important issue that needs to be explored is what observable quantities will be sensitive to the changes in the underlying motion of a physical system. It has been recently shown that the phenomenon of rotational damping observed in rotating nuclei may provide a valuable information on the underlying motion. In the present work, we have investigated the rotational damping and the statistical distribution for measurable quantities in an exactly soluble model with conserved angular momentum. We consider that it is important to make an exact study since any approximation may lead to different errors in the calculation of the rotational damping and the statistical distributions. Consequently, it may not be possible to make a comparison of the two calculated quantities in an accurate manner.

To summarize, in the present work, we have employed the particle-rotor model with particles in a deformed single-j shell of  $i_{13/2}$ , which interact through a two-body delta-interaction. The model has been solved exactly with different input parameters. Within this model space, the present analysis has shown a clear correspondence between the mechanism of rotational damping and the onset of chaos in rotating nuclei. In particular, we have observed the following similarities:

- (1) increase in rotational damping with excitation-energy and the corresponding increase in the degree of chaoticity;
- (2) decrease in rotational damping with increasing angular momentum and the corresponding decrease in the degree of chaoticity;
- (3) decrease in rotational damping with increasing deformation and the corresponding decrease in the degree of chaoticity.

Research at the University of Notre Dame is supported by the NSF under contract number PHY-0140324.

## References

- [1] M.L. Mehta, *Random Matrices*, Academic Press, New York, 1991.
- [2] L.E. Reichl, *The Transition to Chaos*, Springer-Verlag, New York, 1992.
- [3] T. Guhr, A. Müller-Groeling and H.A. Weidenmüller, *Phys. Rep.* **299** (1998) 189.
- [4] O. Bohigas, M.J. Giannoni and C. Schmit, *Phys. Rev. Lett.* **52** (1984) 1.
- [5] R.U. Haq, A. Pandey and O. Bohigas, *Phys. Rev. Lett.* **48** (1982) 1086.
- [6] M. Matsuo, T. Dossing, B. Herskind and S. Frauendorf, *Nucl. Phys.* **A564** (1993) 345.
- [7] A.T. Kruppa, K.F. Pal and N. Rowley, *Phys. Rev.* **C52** (1995) 1818.
- [8] J.A. Sheikh, A.T. Kruppa and N. Rowley, *Nucl. Phys.* **A694** (2001) 233.
- [9] S. Åberg, *Phys. Rev. Lett.* **64** (1990) 3119; *Prog. Part. Nucl. Phys.* Vol. 28 (Pergamon, 1992) p. 11.
- [10] M. Matsuo, T. Dossing, E. Vigezzi and R.A. Broglia, *Phys. Rev. Lett.* **70** (1993) 2694.
- [11] K. Yoshida and M. Matsuo, *Nucl. Phys.* **A612** (1997) 26.
- [12] V. Zelevinsky, B.A. Brown, N. Frazier and M. Horoi, *Phys. Rep.* **276** (1996) 85.
- [13] J.D. Garrett, J.Q. Robinson, A.J. Foglia and H.-Q. Jin, *Phys. Lett.* **B392** (1997) 24.
- [14] M. Matsuo, T. Dossing, E. Vigezzi and S. Åberg, *Nucl. Phys.* **A620** (1997) 296.
- [15] A. Bohr and B. Mottelson, *Nuclear Structure II*, W.A. Benjamin, New York, 1975.
- [16] J.A. Sheikh, D.D. Warner and P. Van Isacker, *Phys. Lett.* **B443** (1998) 16.
- [17] C.G. Andersson and J. Krumlinde, *Nucl. Phys.* **A334** (1980) 486.

- [18] T.A. Brody, J. Flores, J.B. French, P.A. Mello, A. Pandey and S.S.M. Wong, *Rev. Mod. Phys.* **53** (1981) 385.
- [19] O. Bohigas and M.-J. Giannoni, in *Mathematical and Computational Method in Nuclear Physics*, Vol. 209 of *Lecture Notes in Physics*, eds. J. S. Dehesa, J. M. G. Gomez and A. Polls (Springer-Verlag, Berlin, 1984) p. 1.
- [20] T.H. Seligman and J. J. M. Verbaarschot, *J. Phys. A: Math. Gen.* **18** (1985) 2227.
- [21] S.T.W.H. Press, B.P. Flannery and W. Vetterling, *Numerical Recipes*, Cambridge University Press, Cambridge, 1986.

Table 1

The results of the branching number  $n$ , defined in Eq. (11), for the normal deformation case with  $\kappa = 2.5$  MeV. The numbers presented are averaged for ten initial states. For example, the number 1 – 10 in the first column signifies that the values have been averaged for initial eigen-states from 1 to 10.

Initial eigenstates	$I_i = 12 \rightarrow I_f = 10$		$I_i = 32 \rightarrow I_f = 30$		$I_i = 62 \rightarrow I_f = 60$	
	$n_{(Q_0=0)}$	$n_{(Q_0=2.5)}$	$n_{(Q_0=0)}$	$n_{(Q_0=2.5)}$	$n_{(Q_0=0)}$	$n_{(Q_0=2.5)}$
1 – 10	2.09	1.48	2.56	1.35	4.43	1.54
11 – 20	6.96	3.75	5.81	2.41	7.33	1.92
21 – 30	9.79	5.43	8.16	2.76	7.02	2.02
31 – 40	11.77	5.51	9.68	2.54	9.62	1.83
41 – 50	17.41	8.47	14.70	3.78	9.38	1.91
275 – 284	107.16	35.52	70.18	7.18	21.91	4.54
285 – 294	102.19	34.24	61.52	8.92	24.38	3.77
295 – 304	108.24	34.05	69.33	11.56	22.36	3.29
305 – 314	110.05	35.48	64.53	7.94	18.37	4.47
315 – 324	115.78	39.24	65.83	7.78	23.89	4.48
575 – 584	140.82	50.96	79.99	9.79	21.67	5.60
585 – 594	145.62	50.71	73.37	8.18	19.22	2.89
595 – 604	137.70	48.95	63.17	8.36	13.18	3.20
605 – 614	149.51	54.33	71.78	11.52	25.54	2.75
615 – 624	146.49	56.60	64.41	9.37	22.53	3.93

Table 2

The same as Table I, but for the superdeformation case with  $\kappa = 6$  MeV.

Initial eigenstates	$I_i = 12 \rightarrow I_f = 10$		$I_i = 32 \rightarrow I_f = 30$		$I_i = 62 \rightarrow I_f = 60$	
	$n_{(Q_0=0)}$	$n_{(Q_0=5.0)}$	$n_{(Q_0=0)}$	$n_{(Q_0=5.0)}$	$n_{(Q_0=0)}$	$n_{(Q_0=5.0)}$
1 – 10	1.91	1.34	1.68	1.12	2.57	1.06
11 – 20	2.40	1.55	2.74	1.49	4.61	1.36
21 – 30	5.33	2.67	3.51	1.69	6.18	1.65
31 – 40	7.37	3.50	5.13	2.36	6.77	1.39
41 – 50	8.23	3.58	5.82	2.17	6.83	1.50
275 – 284	57.52	15.52	51.89	8.42	25.89	2.53
285 – 294	47.96	10.07	44.85	7.67	29.28	2.35
295 – 304	54.73	11.61	63.29	9.56	27.50	3.03
305 – 314	59.36	10.36	63.47	11.21	40.92	4.02
315 – 324	60.90	14.61	58.97	10.12	36.44	3.19
575 – 584	98.83	16.41	82.31	13.48	40.13	3.25
585 – 594	106.70	20.00	96.13	12.38	29.94	2.45
595 – 604	119.50	14.66	91.19	10.37	35.23	2.97
605 – 614	95.99	14.59	65.22	10.09	34.68	2.69
615 – 624	100.95	13.55	75.04	11.68	23.36	2.14

Fig. 1. The spectral-rigidity parameter of Dyson and Mehta for  $\kappa = 2.5$  MeV for various angular momenta. Three sets of calculations have been carried out. In the first set (shown by filled circle), the analysis have been done with all the eigen-values, in the second case (shown by upper triangle) the eigen-values ranging from 1 to 400 have been used, and in the third case (shown by lower triangle) the eigen-values from 401 to 800 have been selected.

Fig. 2. The same as in Figure 1, but for  $\kappa = 6$  MeV.

Fig. 3. The normalised B(E2) transition probabilities obtained for  $\kappa = 2.5$  MeV with no core quadrupole moment,  $Q_0 = 0$ . The results are shown for the transitions (a)  $I_i = 12 \rightarrow I_f = 10$ , (b)  $I_i = 32 \rightarrow I_f = 30$  and (c)  $I_i = 62 \rightarrow I_f = 60$ . For each case, the transition probability is given for three different initial eigen-states of  $i = 26, 300$  and  $600$ .

Fig. 4. The same as in Figure 3, but for  $\kappa = 2.5$  MeV with core quadrupole moment,  $Q_0 = 2.5$  barn.

Fig. 5. The same as in Figure 3, but for  $\kappa = 6.0$  MeV with no core quadrupole moment,  $Q_0 = 0$ .

Fig. 6. The same as in Figure 3, but for  $\kappa = 6.0$  MeV with core quadrupole moment,  $Q_0 = 5.0$  barn.

Fig. 7. Density of states as a function of excitation energy. Calculations are performed for three representative angular momenta  $I = 10, 30$ , and  $60$ , and for the two deformations  $\kappa = 2.5$  and  $6$  MeV.

Fig. 8. The same as in Figure 5, but with enhanced residual interaction.

Fig. 9. The same as in Figure 6, but with enhanced residual interaction.

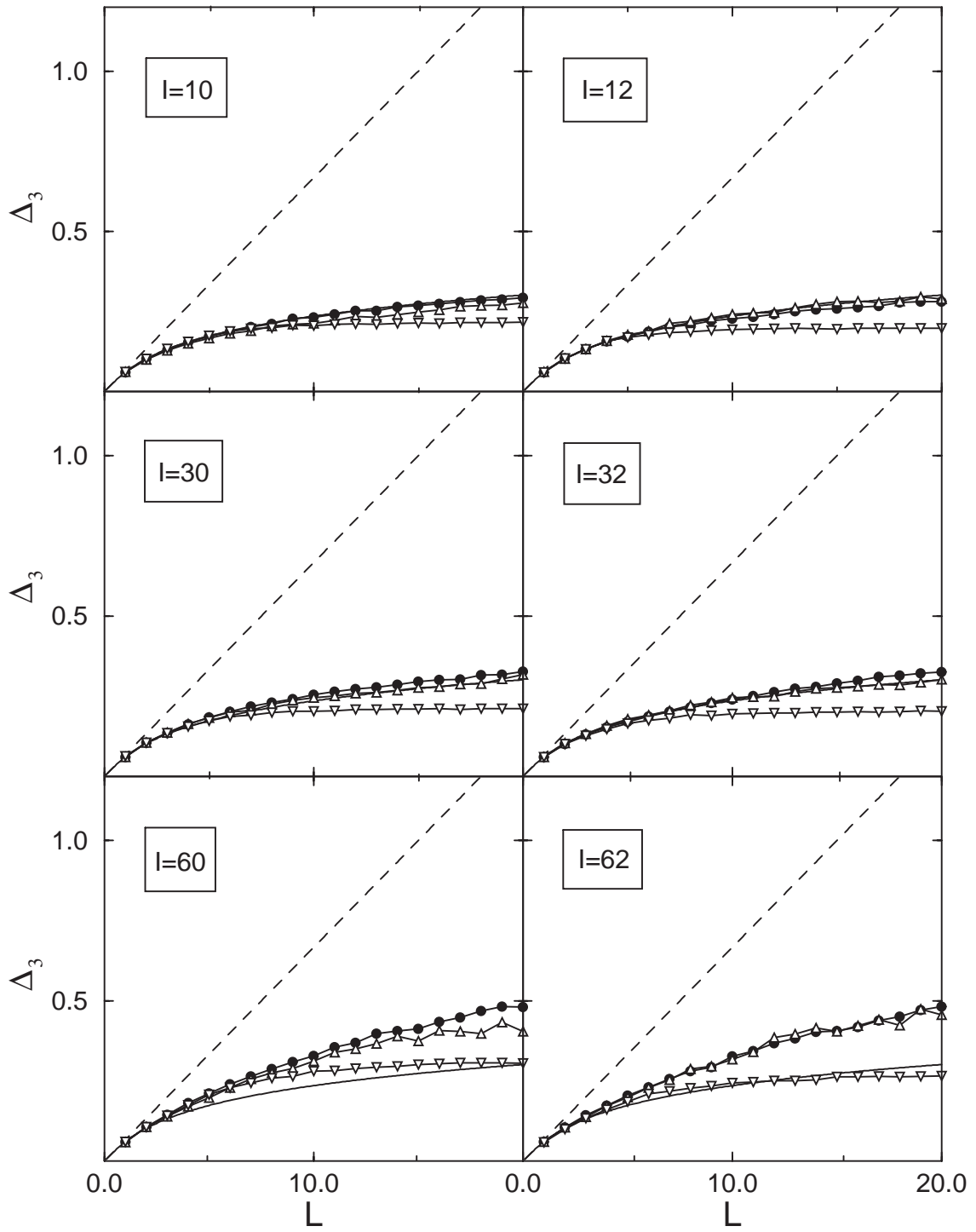


Fig. 1, Sheikh and Sun



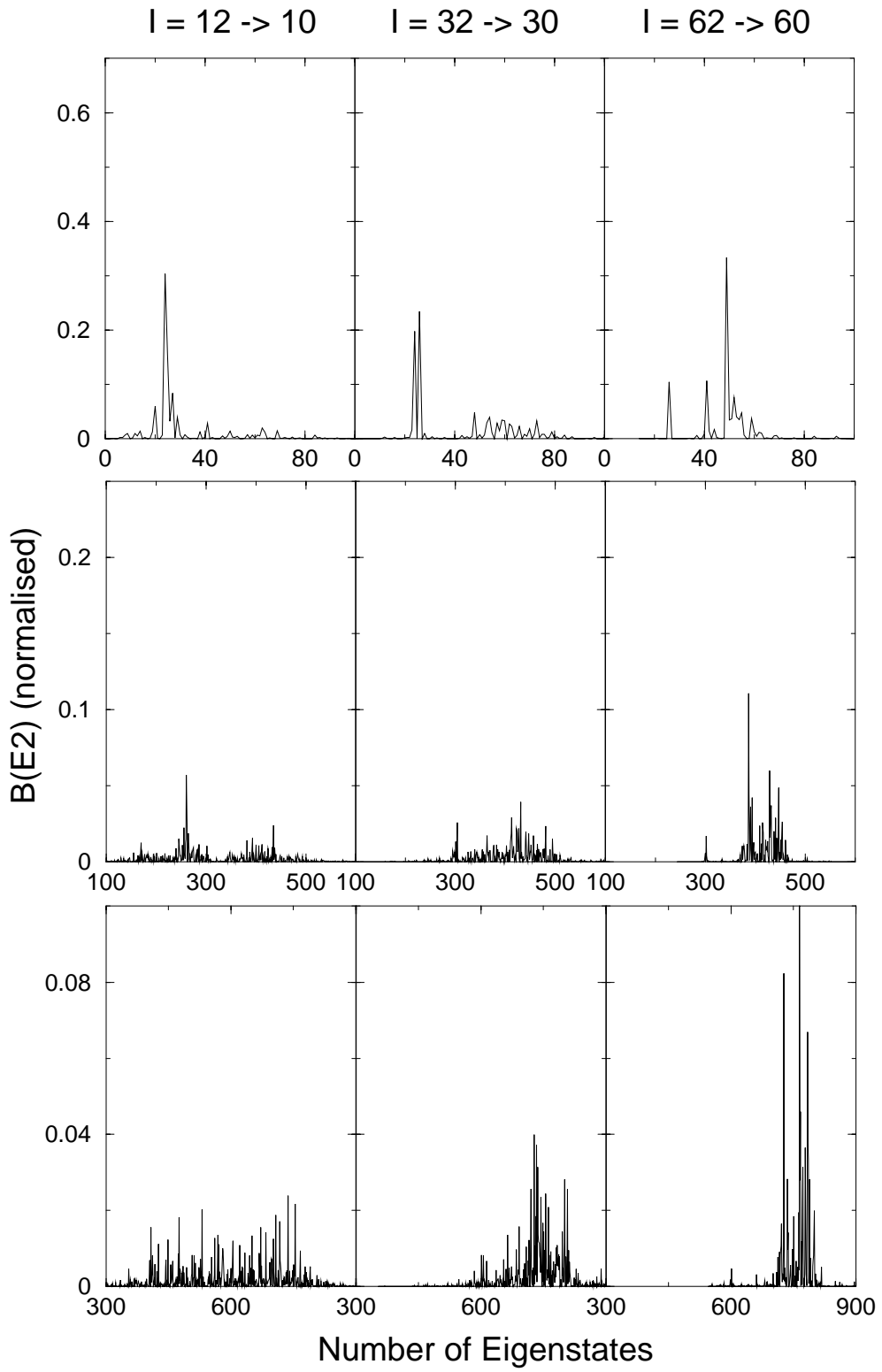


Fig. 3, Sheikh and Sun

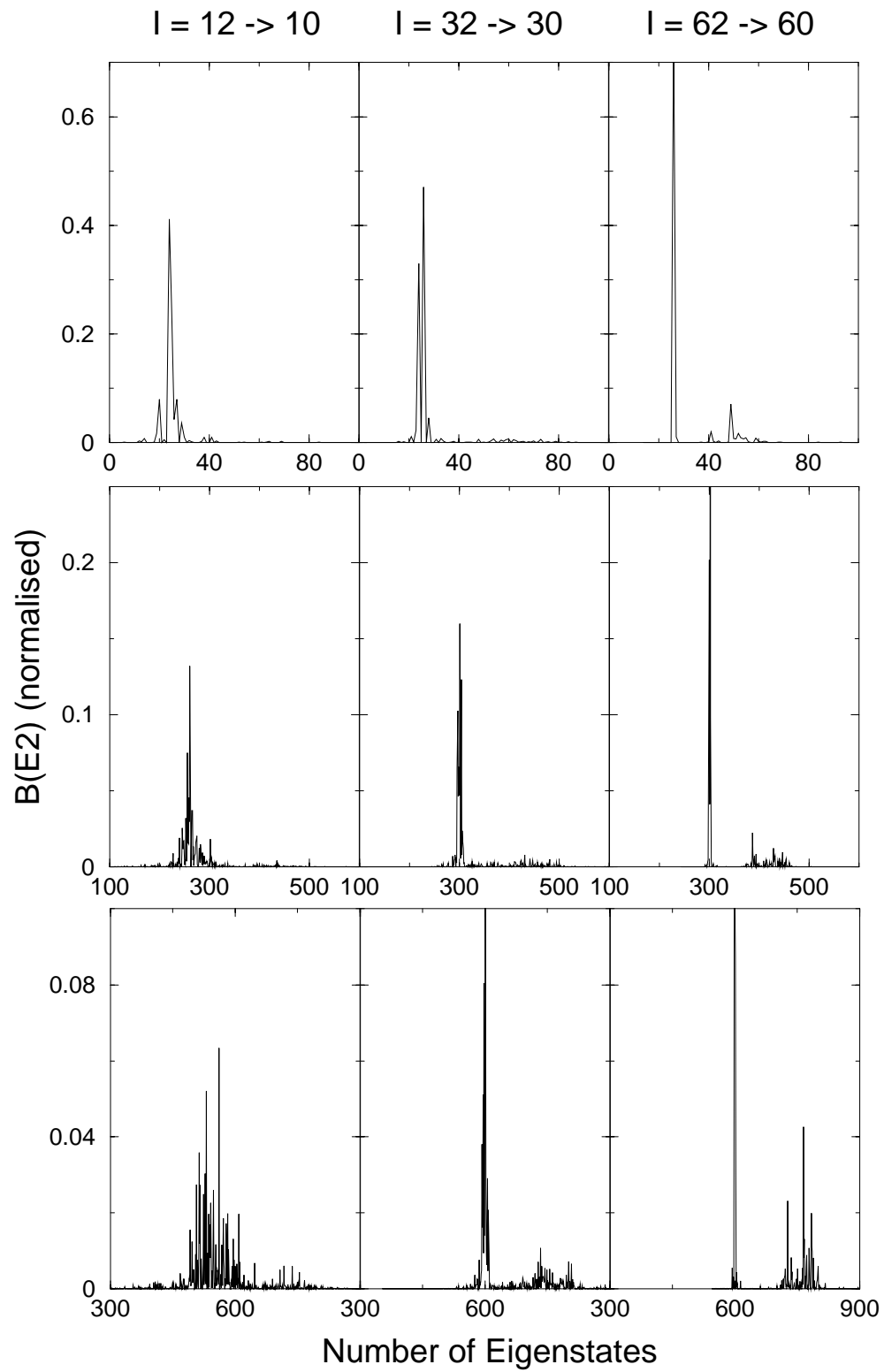


Fig. 4, Sheikh and Sun

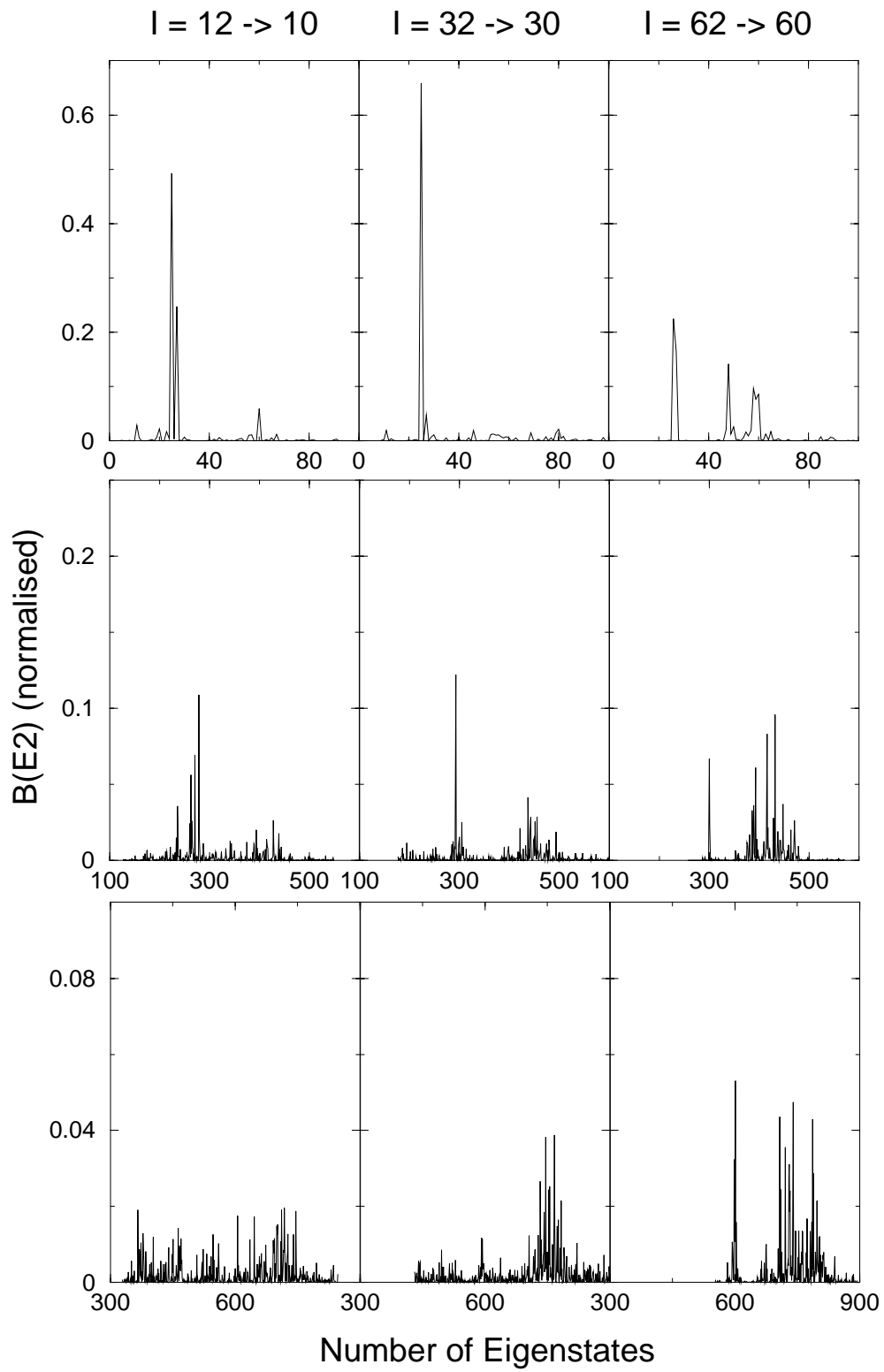


Fig. 5, Sheikh and Sun

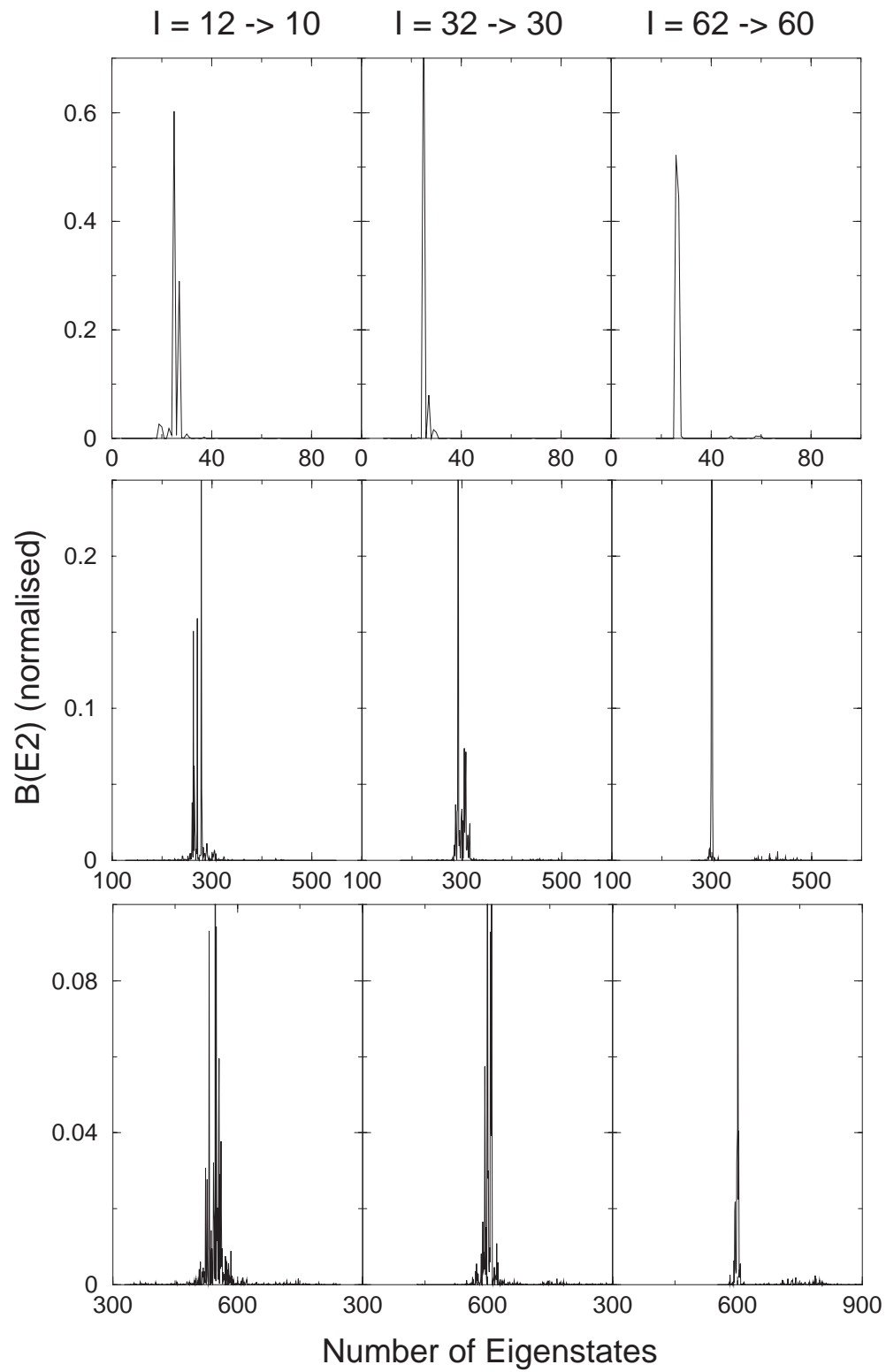


Fig. 6, Sheikh and Sun

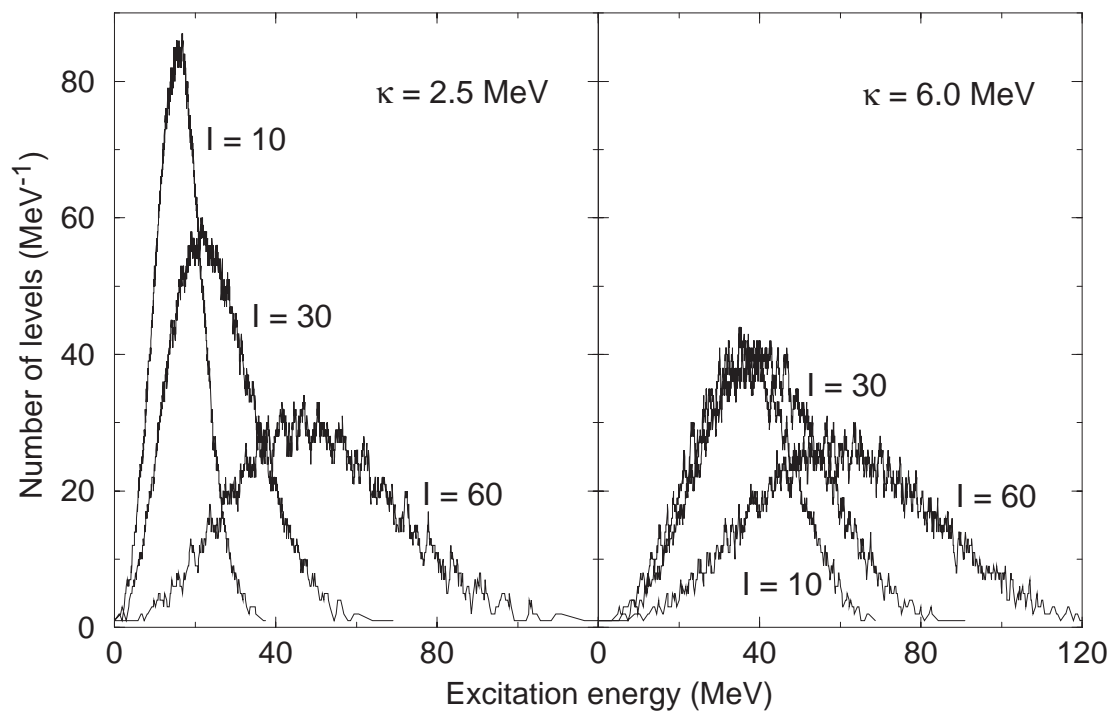


Fig. 7, Sheikh and Sun

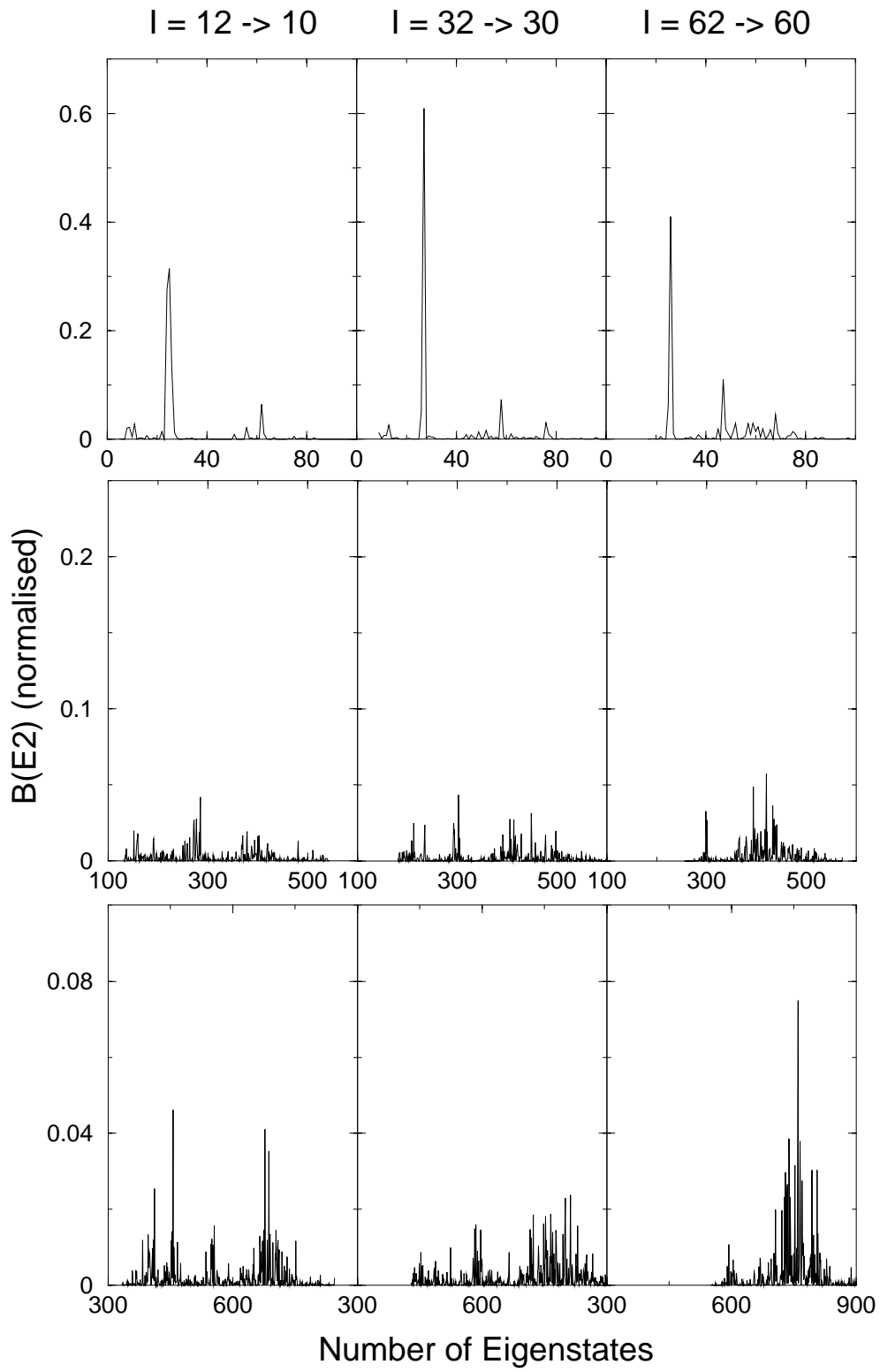


Fig. 8, Sheikh and Sun

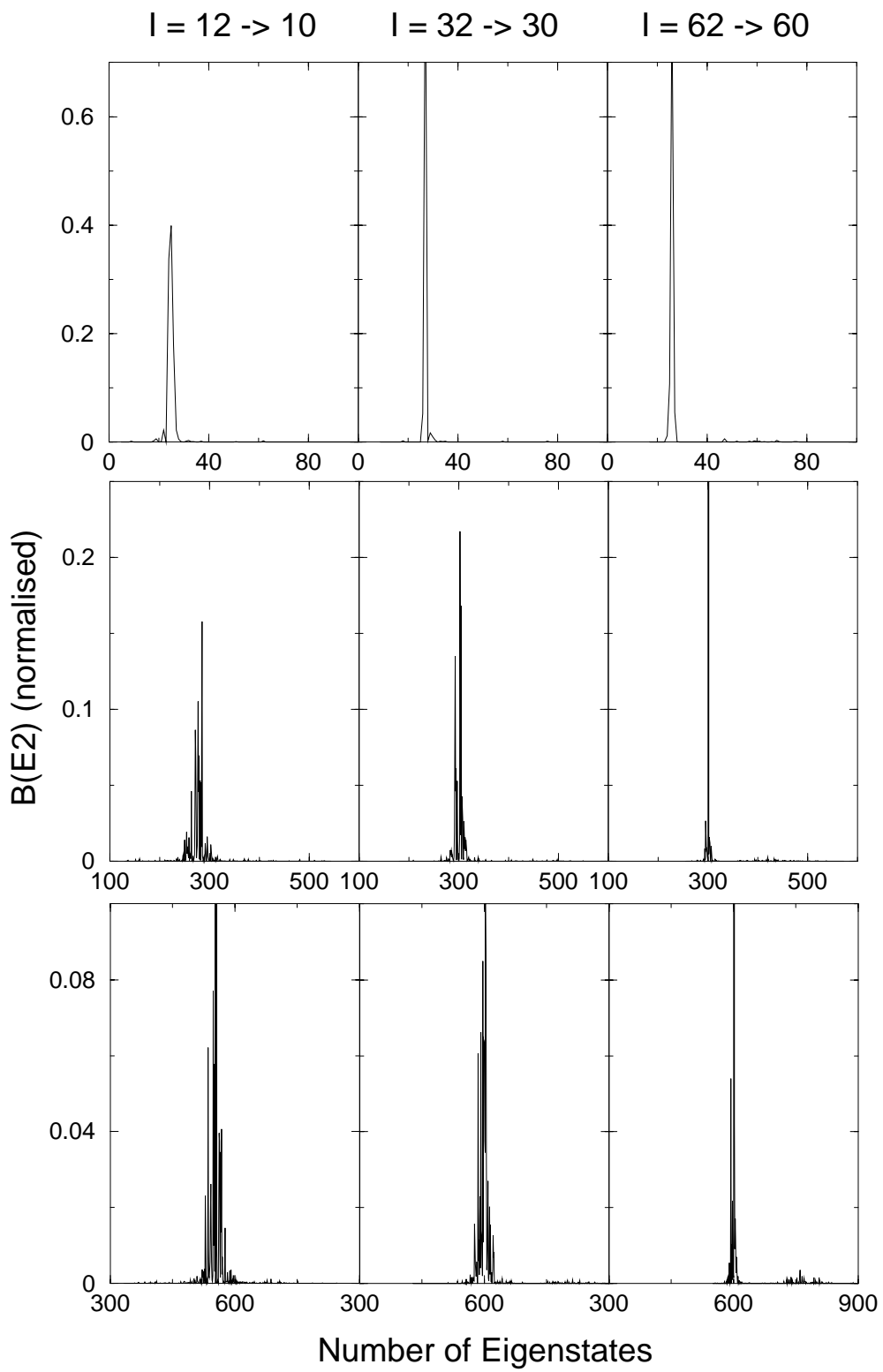


Fig. 9, Sheikh and Sun